

# Exploring the XPS limit in soft and hard x-ray angle-resolved photoemission using a temperature-dependent one-step theory

J. Braun,<sup>1</sup> J. Minár,<sup>1</sup> S. Mankovsky,<sup>1</sup> V. N. Strocov,<sup>2</sup> N. B. Brookes,<sup>3</sup> L. Plucinski,<sup>4,5</sup>  
C. M. Schneider,<sup>4,5</sup> C. S. Fadley,<sup>6,7</sup> and H. Ebert<sup>1</sup>

<sup>1</sup>*Department Chemie, Ludwig-Maximilians-Universität München, 81377 München, Germany*

<sup>2</sup>*Swiss Light Source, Paul Scherrer Institut, CH 5232 Villigen, PSI, Switzerland*

<sup>3</sup>*European Synchrotron Radiation Facility (ESRF), Bote Postale 220, 38043 Grenoble, France*

<sup>4</sup>*Peter Grünberg Institut PGI-6, Forschungszentrum Jülich, 52425 Jülich, Germany*

<sup>5</sup>*Fakultät für Physik, Universität Duisburg-Essen, 47048 Duisburg, Germany*

<sup>6</sup>*Materials Sciences Division, Lawrence Berkeley National Laboratory, Berkeley, California 04720, USA*

<sup>7</sup>*Department of Physics, University of California Davis, Davis, California 95616, USA*

(Received 21 February 2013; revised manuscript received 15 October 2013; published 7 November 2013)

We present a theory of temperature-dependent photoemission which accurately describes phonon effects in soft and hard x-ray angle-resolved photoemission. Our approach is based on a fully relativistic one-step theory of photoemission that quantitatively reproduces the effects of phonon-assisted transitions beyond the usual  $\mathbf{k}$ -conserving dipole selection rules which lead to the so-called XPS limit in the hard x-ray and/or high temperature regime. Vibrational atomic displacements have been included using the coherent potential approximation in analogy to the treatment of disordered alloys. The applicability of this alloy analogy model is demonstrated by direct comparison to experimental soft x-ray data from W(110) showing very satisfying agreement.

DOI: [10.1103/PhysRevB.88.205409](https://doi.org/10.1103/PhysRevB.88.205409)

PACS number(s): 71.20.-b, 79.60.-i

## I. INTRODUCTION

Angle-resolved photoemission (ARPES) has developed over the past several decades into the technique of choice for determining the electronic structure of any new crystalline material, and it is thus in some respects a very mature tool in materials physics.<sup>1,2</sup> It has always been realized, however, that the results obtained are restricted in sensitivity to the near surface of the systems studied, due to the short inelastic mean free paths (IMFPs) of  $\sim 5$ – $10$  Å of the low energy photoelectrons, which are typically in the range from 10 to 150 eV.<sup>3</sup> To overcome this limitation of surface sensitivity, there is now considerable interest in using higher energy x rays in the soft x-ray sub-keV or even hard x-ray multi-keV regime to access deeper-lying layers in a sample, thus sampling more bulklike properties.<sup>4–21</sup> One can thus think of soft x-ray ARPES (SARPES) or hard x-ray ARPES (HARPES), respectively. These techniques have to date been applied to a wide variety of materials, including free-electron and transition metals,<sup>4,11</sup> strongly correlated oxides and high  $T_C$  materials,<sup>6,7</sup> heavy fermion systems,<sup>6</sup> mixed-valent Ce compounds,<sup>9</sup> dilute magnetic semiconductors,<sup>16,19,21</sup> layered transition metal dichalcogenides,<sup>15</sup> and bulk and Rashba phenomena.<sup>17</sup> Additional advantages in such experiments are being able to tune to core-level resonances so as to identify the atomic-orbital makeup of ARPES features,<sup>21</sup> to map three-dimensional Fermi surfaces,<sup>15</sup> and to take advantage of the longer IMFPs, which translate into less smearing of dispersive features along the emission direction (usually near the surface normal).<sup>14</sup>

Going higher in energy however comes with some additional challenges for interpretation of the data.<sup>4,10,14</sup> Deviations from the dipole approximation in photoelectron excitation mean that the momentum of the photon can result in a non-negligible shift of the position of the initial-state wave vector in the reduced Brillouin zone (BZ), as first pointed out some time ago. Phonon creation and annihilation during photoemission

also hinders the unambiguous specification of the initial state in the BZ via wave vector conservation.<sup>4,5,10,11,13,14,16</sup> Following Shevchik,<sup>22</sup> the photoemission intensities at a given energy  $E$  and vector  $\mathbf{k}$  can be approximately divided into zero-phonon direct transitions  $I^{\text{DT}}(E, \mathbf{k})$  and phonon-assisted nondirect transitions  $I^{\text{NDT}}(E, \mathbf{k})$ . As a rough guide to the degree of direct-transition behavior expected in an ARPES experiment, one can use a temperature-dependent Debye-Waller factor  $W(T)$  which qualitatively represents the fraction of direct transitions.<sup>4,5,10,14,22–24</sup> As a first approach that aimed to go beyond this simple scheme for temperature-dependent ARPES, Larsson and Pendry<sup>25</sup> introduced a model called Debye-Waller model later on which incorporates the effect of lattice vibrations on the photoemission matrix elements. More than 15 years later Zampieri *et al.*<sup>26</sup> introduced a cluster approach to model the temperature-dependent excitation of valence band electrons for photon energies of about 1 keV. More recently Fujikawa and Arai<sup>27,28</sup> discussed phonon effects on ARPES spectra on the basis of nonequilibrium Green's function theory. However, to date no truly quantitative and generally applicable model has been developed for predicting these phonon effects in ARPES.

We present an approach which accurately models phonon effects over the full energy range from normal low-energy ARPES to HARPES. More importantly it converges for high temperatures and/or photon energies to the so called XPS limit in photoemission, in particular the development of matrix-element-weighted density-of-states (MEW-DOS)-like features in the intensity distribution.<sup>13,29</sup> Our alloy analogy model includes vibrational atomic displacements via the coherent potential approximation (CPA), where vibrations of different lattice sites are assumed to be uncorrelated and averaged in the sense of CPA over various possible displacements which are calculated within Debye theory. Using the CPA formulation of the one-step model<sup>30–32</sup> provides a self-consistent temperature-

dependent averaging of the photoemission matrix elements. In other words, we describe in a quantitative sense the breakdown of the  $\mathbf{k}$ -conserving rules due to phonon-assisted transitions, the driving mechanism that leads finally to the XPS limit.

## II. CALCULATION OF THE CPA PHOTOCURRENT AT FINITE TEMPERATURES

Based on the CPA approach for configurational averaging the temperature-dependent photocurrent at a given final-state energy  $\epsilon_f$ , wave vector  $\mathbf{k}$ , and temperature  $T$  follows to

$$\langle I^{\text{AR-PES}}(\epsilon_f, \mathbf{k}, T) \rangle = \langle I^{\text{at}}(\epsilon_f, \mathbf{k}, T) \rangle + \langle I^{\text{s}}(\epsilon_f, \mathbf{k}, T) \rangle + \langle I^{\text{ms}}(\epsilon_f, \mathbf{k}, T) \rangle + \langle I^{\text{inc}}(\epsilon_f, \mathbf{k}, T) \rangle, \quad (1)$$

again with contributions from a pure atomic part, a coherent part with multiple scattering involved, a surface-layer contribution, and an incoherent part.<sup>30,31</sup>

By contrast, the temperature-dependent version of the angle-integrated photocurrent is given by

$$\langle I^{\text{AI-PES}}(\epsilon_f, \mathbf{k}, T) \rangle = \langle I^{\text{at}}(\epsilon_f, \mathbf{k}, T) \rangle + \langle I^{\text{s}}(\epsilon_f, \mathbf{k}, T) \rangle + \langle I^{\text{inc}}(\epsilon_f, \mathbf{k}, T) \rangle. \quad (2)$$

In the XPS limit it follows:

$$\langle I^{\text{ms}}(\epsilon_f, \mathbf{k}, T) \rangle \rightarrow 0, \quad (3)$$

because the temperature-dependent single-site scattering matrix smears out all dispersive features, which are related to the multiple scattering part, and results in a smooth background that extrapolates to zero for high temperatures and/or photon energies. In consequence, the XPS limit is given by

$$\langle I^{\text{AR-PES}}(\epsilon_f, \mathbf{k}, T) \rangle \rightarrow \langle I^{\text{AI-PES}}(\epsilon_f, \mathbf{k}, T) \rangle. \quad (4)$$

In our approach we include the vibrational atomic displacements via the CPA, where vibrations of different lattice sites are assumed to be uncorrelated. For example, a set of 14 different modes may be used to represent the thermal vibrations of a simple fcc or bcc lattice. For these vibrational displacements the CPA average has to be taken over for a given temperature  $T$ . Using for the explicit calculation Debye theory, a certain temperature-dependent distribution function  $P(\Delta \mathbf{R}_n, T)$ , the probability  $P$  of a certain vibrational displacement  $\Delta \mathbf{R}_n$  as a function of  $T$  results. This finally provides us with the temperature-dependent single-site scattering matrix<sup>23</sup> which can be embedded in the one-step formalism.<sup>33</sup> This means that the coherent temperature-dependent single-site scattering matrix enters the spin-polarized low energy electron diffraction (SPLEED) formalism as usual. Calculations based on this approach have been used to successfully interpret ARPES data over the full energy spectrum in recent years.<sup>10,13,16,18,33</sup> The CPA formulation of the one-step model<sup>30,31</sup> allows for a self-consistent temperature-dependent averaging of the photoemission matrix elements, in contrast to previous work which simplified the problem to temperature-dependent scattering phase shifts only.<sup>23,33</sup>

Furthermore, we can calculate the amplitudes for all possible displacements and the corresponding displacement matrices.<sup>34</sup> The corresponding CPA-projector matrices allow for the explicit CPA averaging as shown in the last section and

the temperature dependence of the different contributions is described by the set of displacement matrices. The temperature dependence of the atomic contributions results in

$$\langle I^{\text{at}}(\epsilon_f, \mathbf{k}, T) \rangle \propto \text{Im} \sum_{\substack{jn\alpha_n \\ \Lambda\Lambda'}} A_{jn\Lambda}^c \mathcal{Z}_{jn\alpha_n}^{\text{at}}(T) A_{jn\Lambda'}^{c*}, \quad (5)$$

with

$$\mathcal{Z}_{jn\alpha_n}^{\text{at}}(T) = \sum_{\substack{v_n \\ \Lambda''\Lambda'''}} x_{jn\alpha_n v_n} U_{v_n}(T) \mathcal{Z}_{jn\alpha_n}^{\text{at}} U_{v_n}^\dagger(T). \quad (6)$$

Herein the matrix  $U_{v_n}$  represents a certain displacement calculated for a given temperature  $T$  with  $U_{v_n}^\dagger$  being the adjoint matrix. Again, the indices  $n$  and  $j$  denote the  $n$ th atomic cell and the  $j$ th layer. The corresponding weight for a given species  $\alpha_n$  and/or displacement  $v_n$  at site  $n$  is given by  $x_{jn\alpha_n v_n}$ .  $A_{jn}^c$  denote the coherent spherical coefficients of the final-state wave field and the matrix  $\mathcal{Z}^{\text{at}}$  consists of radial double matrix elements combined with corresponding angular parts. A detailed description of the multiple scattering coefficients  $A_{jn}^c$  and of the matrix  $\mathcal{Z}^{\text{at}}$  is given in Ref. 33. The temperature-dependent averaging of the coherent and incoherent multiple scattering contributions is done in an analogous way.

The temperature dependence of the coherent matrices  $\mathcal{Z}^{c(1)}$  and  $\mathcal{Z}^{c(2)}$  is defined as

$$\mathcal{Z}_{jn}^{c(1)}(T) = \sum_{\substack{\alpha_n \\ \Lambda_1\Lambda_2\Lambda_3}} U_{v_n}(T) \mathcal{Z}_{jn\alpha_n}^{c(1)} U_{v_n}^\dagger(T), \quad (7)$$

with

$$\mathcal{Z}_{jn\alpha_n}^{c(1)} = \sum_{\substack{\alpha_n \\ \Lambda_1\Lambda_2\Lambda_3}} x_{jn\alpha_n v_n} D_{jn\alpha_n}^\dagger R_{jn\alpha_n}^{(1)} D_{jn\alpha_n}. \quad (8)$$

For  $\mathcal{Z}^{c(2)}$  it follows:

$$\mathcal{Z}_{jn}^{c(2)}(T) = \sum_{\substack{\alpha_n \\ \Lambda_1\Lambda_2\Lambda_3}} U_{v_n}(T) \mathcal{Z}_{jn\alpha_n}^{c(2)} U_{v_n}^\dagger(T), \quad (9)$$

with

$$\mathcal{Z}_{jn\alpha_n}^{c(2)} = \sum_{\substack{\alpha_n \\ \Lambda_1\Lambda_2\Lambda_3}} x_{jn\alpha_n v_n} D_{\Lambda_1\Lambda_2} R_{jn\alpha_n}^{(2)} D_{\Lambda_3\Lambda_1}. \quad (10)$$

Finally, it remains to describe the temperature dependence of the incoherent part of the photocurrent. The last term in Eq. (1) is still temperature dependent because it is defined via the coherent matrices  $\mathcal{Z}^{c(1)}(T)$  and  $\mathcal{Z}^{c(2)}(T)$ . The first term denotes the incoherent contributions of the different species and/or displacements. Therefore, it follows for the temperature dependence of the complete incoherent part:

$$\begin{aligned} \langle I^{\text{inc}}(\epsilon_f, \mathbf{k}, T) \rangle &\propto \text{Im} \sum_{\substack{jn \\ \Lambda\Lambda'}} A_{jn\Lambda}^c \mathcal{Z}_{jn}^{c(1)}(T) \tau_{cjn}^{00} \mathcal{Z}_{jn}^{c(2)}(T) A_{jn\Lambda'}^{c*} \\ &+ \text{Im} \sum_{\substack{jn \\ \alpha_n v_n \\ \Lambda\Lambda'}} x_{jn\alpha_n v_n} A_{jn\Lambda}^c \mathcal{Z}_{jn\alpha_n}^{(3)}(T) A_{jn\Lambda'}^{c*}, \end{aligned} \quad (11)$$

with

$$\begin{aligned} \mathcal{Z}_{jn\alpha_n}^{(3)}(T) = & \sum_{\substack{\Lambda''\Lambda''' \\ \Lambda'''\Lambda''''}} U_{v_n}(T) \mathcal{Z}_{jn\alpha_n}^{(1)} \\ & * (\tau_{jn\alpha_n}^{00} - t_{jn\alpha_n})_{\Lambda'''\Lambda''''} \\ & * \mathcal{Z}_{jn\alpha_n}^{(2)} U_{v_n}^\dagger(T). \end{aligned} \quad (12)$$

The temperature-dependent averaging of the incoherent part  $\langle I^{\text{inc}}(\epsilon_f, \mathbf{k}, T) \rangle$  completes the CPA-averaged photocurrent at finite temperatures. The calculation of the CPA-averaged photocurrent at  $T = 0$  K is shown in the Appendix. In a similar way, thermal displacements of atoms were successfully introduced by some of us within the alloy analogy model to calculate the Gilbert damping parameter.<sup>35,36</sup> This approach has been implemented in the CPA version of the one-step model,<sup>34</sup> with the latter having been extended to higher photon energies before.<sup>10,13,16,18,29,34,37–39</sup>

### III. DISCUSSION

As a first illustration of the effect of phonon-assisted transitions on ARPES, we consider intensity distributions calculated in a fully relativistic way for Au(111) as a function of temperature and excitation energy. Au is chosen as a typical transition metal with a low Debye temperature of  $\Theta_D = 165$  K. The calculated results for two different photon energies of 1.0 and 6.4 keV are presented in Fig. 1. Considering first 1 keV, the left panel shows angle-resolved intensity distributions for normal emission that are labeled AR-PES (red curves) in comparison to  $2\pi$  angle-integrated (AI-PES) intensities (blue curves) at 10, 100, and 300 K. The AI-PES curves

are expected to very closely represent XPS-limit MEW-DOS results, even at zero temperature, and thus to be only weakly dependent on temperature. This is because the spectral line shapes reflect to a good approximation the MEW-DOS for all temperatures. The main impact of temperature is therefore a Debye-Waller-like decrease of angle-resolved-like features, and an increase of the relatively constant MEW-DOS spectrum. As expected, these two spectral distributions strongly deviate from one another as a function of binding energy at low temperature. For higher temperatures, the overall shape of the AR spectra significantly changes, whereas the AI spectra show only small deviations in their intensity profiles. In the AI-PES results we see only the phonon-assisted transitions producing small temperature-dependent changes in the matrix elements. The situation is completely different in the angle-resolved case. The temperature-dependent matrix elements are responsible for a decrease of the angle-resolved intensity profiles due to a redistribution of spectral weight. This mechanism, associated with a Debye-Waller-like suppression of the direct part of the photocurrent is primarily responsible for the so called XPS limit in ARPES, which clearly shows up in the left panel of Fig. 1 for 1 keV photon energy at 300 K. Final state energy broadening due to lifetime effects and phonon creation/annihilation that are not included in our calculations support this DOS-like transformation of spectral weight<sup>22</sup> and cause additional smearing of dispersing features. The first effect is naturally included in our photoemission calculations for the final state due to the use of a time-reversed LEED state<sup>40</sup> with a finite inelastic mean-free path. Multiphonon induced effects are not included in our theory but according to Shevchik<sup>22</sup> one should expect an additional smearing of about 0.2 eV, which would alter the calculated spectra only slightly via a corresponding energy broadening.

Turning now to the right panel of Fig. 1 with an excitation energy of 6.4 keV, we see more dramatic effects at lower temperature, with the XPS limit being reached already by 100 K. This behavior was observed, for example, in recent HARPES measurements on W(110) and GaAs(100).<sup>13</sup> For 6.4 keV excitation of the valence electrons, the Debye-Waller factor of Au is about 0.45 at 30 K, and about 0.09 at 300 K, which means that only 9% direct transitions should survive at 6.4 keV at room temperature. This kind of analysis leads to the need for cryogenic cooling to minimize phonon induced effects in soft and hard angle-resolved x-ray experiments. Nevertheless, these effects are still present in the experimental data, even at low temperatures. This makes it more difficult to achieve an accurate picture of the bulk electronic structure and indicates the importance of interpreting data via our more realistic model.

As a second system, we consider Pt, again a heavy 5d metal, adjacent to Au and with very nearly the same atomic mass (195.1 u versus 197.0 u for Au), but with a much higher Debye temperature of  $\Theta_D = 230$  K, which leads to higher Debye-Waller factors than Au and thus to a preservation of dispersing features up to higher temperatures and/or photon energies. The left panel of Fig. 2 again presents calculated soft x-ray angle-resolved spectra for 1 keV excitation, this time for 10, 100, 300, and 500 K. In contrast to the spectra calculated for Au a much higher temperature is needed to reach the XPS limit at 1 keV for Pt. Even at 300 K dispersing features survive

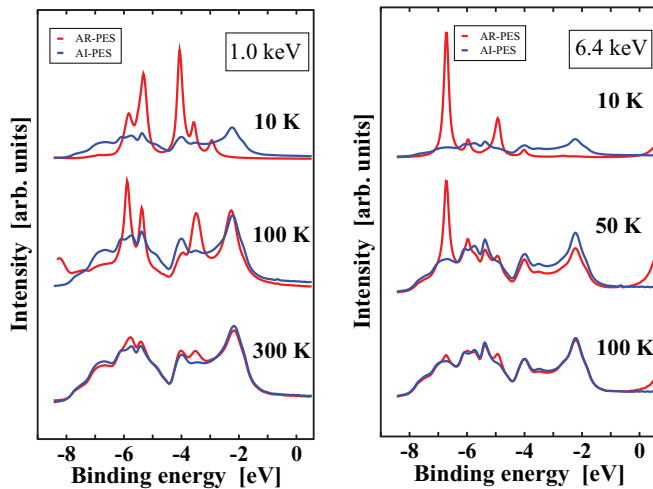


FIG. 1. (Color online) Calculated photoemission spectra for Au(111) at two different excitation energies as a function of temperature. Shown is the comparison between normal emission angle-resolved data (AR-PES, red curves) and corresponding angle-integrated calculations (AI-PES, blue curves). Left panel: Intensity distributions for an excitation energy of 1.0 keV for three temperatures of 10, 100, and 300 K. Right panel: As the left panel, but for an excitation energy of 6.4 keV and a selection of lower temperatures of 10, 50, and 100 K.



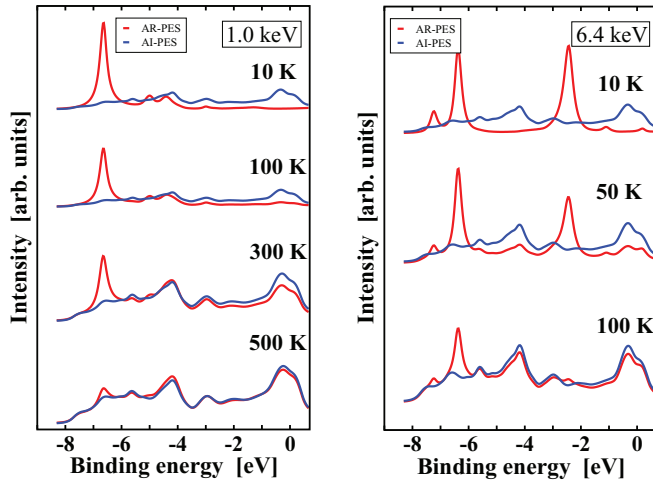


FIG. 2. (Color online) As Fig. 1, but for Pt(111) and for four different temperatures of 10, 100, 300, and 500 K as in Fig. 1 at  $h\nu = 1.0$  keV (left panel). The same three temperatures are shown for  $h\nu = 6.4$  keV (right panel).

at higher binding energies in the soft x-ray spectra. In the right panel of Fig. 2 for 6.4 keV excitation, analogous results are shown for three lower temperatures of 10, 50, and 100 K, and they clearly reveal that by comparison with Au one has to increase the temperature to values far beyond 100 K to generate EDCs which look essentially MEW-DOS-like in their line shapes.

As a final comment, we note that, if the AI-PES curves in either Fig. 1 or Fig. 2 are normalized to the same maximum height, they are essentially identical, within about 5%, for each photon energy, and are in fact also nearly identical between the two energies for both Au and Pt. This suggests that the matrix elements as averaged over emission angle, which are expected to be dominated by the  $5d$  character of the initial states for both energies, change very little over the valence bands with photon energy, which is consistent with these levels behaving overall as corelike  $5d$  emission described by one cross section, and affected only by XPD in their angular profiles.<sup>13,26</sup>

In Fig. 3 we now compare our calculations directly to experimental data from W(110) with soft x-ray excitation at 870 eV.<sup>10</sup> W has a Debye temperature of 400 K and an atomic mass of 183.84 u near to Au and Pt. In Fig. 3(i) we show experimental results for four different sample temperatures: (a) 300 K, (b) 470 K, (c) 607 K, and (d) 780 K.<sup>10</sup> For all four temperatures dispersive features are clearly seen but with significant smearing and an increase of MEW-DOS-like intensity features as temperature is raised. Also shown in Figs. 4(a) and 4(b) are vertical and horizontal cuts, respectively, through the 2D data of Fig. 3(i). These cuts yield 4(a)-energy distribution curves (EDCs) and 4(b)-momentum distribution curves (MDCs) to illustrate more directly the changes in both types of distributions with temperature. Also, various spectral features are labeled by the numbers 1–6 in these figures. Figure 3(ii) again presents fully relativistic one-step calculations which are done with our new approach, whereas Fig. 3(iii) shows conventional one-step calculations in which phonon excitations are more simply considered through a temperature-dependent single-site scattering matrix.<sup>24</sup> Although at the

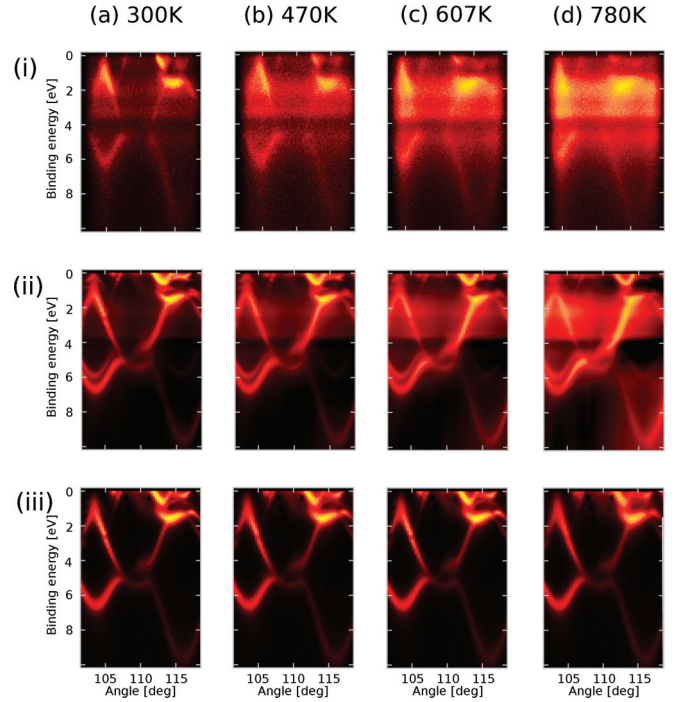


FIG. 3. (Color online) (i) Plots of measured intensity versus angle of emission for 870 eV excitation from the valence bands of W(110) approximately along the  $\Gamma$ -N direction for four temperatures of (a) 300 K, (b) 470 K, (c) 607 K, and (d) 780 K (from Ref. 5), where 90 deg corresponds to normal emission. (ii) Corresponding intensity distributions calculated from temperature-dependent one-step theory based on the CPA formulation. (iii) Conventional ARPES calculations of the direct contribution  $I^{DT}(E, \mathbf{k})$  by use of complex scattering phase shifts and the Debye-Waller model (from Ref. 5).

lowest temperature of 300 K, the two different theoretical approaches yield very similar results, as expected with a Debye-Waller factor of 0.70, the temperature dependence of the experimental data is much better described by our temperature-dependent one-step calculations. The simpler calculation based on the single-site scattering matrix predicts neither the smearing of dispersing features nor the growth of MEW-DOS features for higher binding energies, but shows instead only the expected decrease of direct transition intensities.<sup>10</sup>

Phonon induced smearing only appears via temperature-dependent matrix elements which cause a decrease of the direct part of the photocurrent due to a redistribution of spectral weight. Although for 780 K and a 870 eV photon energy the XPS limit is not fully established for W, the indirect contribution of the temperature-dependent CPA-like photocurrent dominates the corresponding angle-resolved soft x-ray spectra. This is clearly observable from both the experimental and theoretical data, which are nearly in quantitative agreement.

Figures 4(a) and 4(c) compare in more detail the temperature dependence of experimental and theoretical spectra in the form of EDCs for a fixed angle of  $\approx 104$  deg, which is 14 deg from the surface normal. Figures 4(b) and 4(d) present the same comparison for MDCs at a fixed binding energy of  $\approx 2$  eV. The points labeled 1, 2, 4, 5, and 6 denote  $d$ -like electronic states, whereas point 3 labels bands that are more

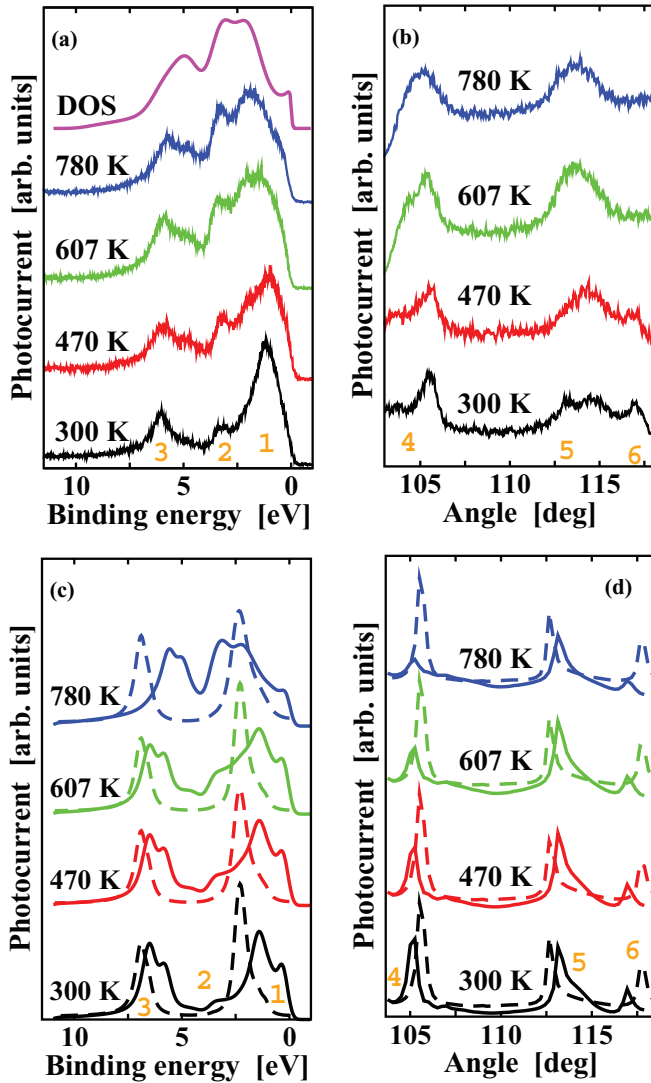


FIG. 4. (Color online) (a) Measured temperature-dependent energy distribution curves (EDCs) as integrated over 20 channels in angle over the windows indicated in Fig. 3(i)-(a-d). A comparison to the W density of states, as broadened by experimental resolution of 400 meV is also shown in the topmost curve. (b) Measured temperature-dependent momentum distribution curves (MDCs) integrated over a narrow energy interval, again as indicated in Fig. 3(i)-(a-d). (c) and (d) Corresponding theoretical results for (c) EDCs and (d) MDCs. Dashed lines indicate conventional one-step calculations, solid lines indicate calculations within the new approach.

free-electron like and a mixture of  $s$  and  $d$  states. The experimental and theoretical data in Fig. 4 show pronounced smearing of features in both EDCs and MDCs as the temperature is raised, but some remnant direct-transition behavior is clearly still present, even at 780 K. The dashed lines shown in Figs. 4(c) and 4(d) indicate conventional one-step calculations using the one-site scattering matrix approach. As expected, only slight changes appear in the form of the EDCs and MDCs as a function of temperature. In contrast, the EDCs and MDCs strongly depend on temperature when using the alloy analogy approach, although in general the MDCs in experiment and those of both the conventional and CPA approaches change less than the EDCs. Significant broadening of spectral features and

shift of spectral weight, not at all present in the conventional one-site scattering matrix approach, can be observed. The EDC at the highest temperature has not converged to a MEW-DOS-like curve and the corresponding MDC still has structure in it. In the XPS limit all MDCs would exhibit only x-ray photoelectron diffraction (XPD), with a different type of angular distribution.<sup>10,16,18,26,29</sup> This is obviously not the case. This is expected because the Debye-Waller factor of 0.41 at 780 K indicates that a certain number of transitions should still be direct. Our calculations thus correctly predict a diminution of the features expected due to direct transitions, and as well a significant broadening of features in the EDCs or MDCs. The additional weak and smooth background observed in the experimental data thus must be ascribed to additional phonon effects, perhaps through multiple phonon excitations.

#### IV. SUMMARY

In summary, we have presented a unique theory of temperature-dependent photoemission that works quantitatively for soft and hard x-ray photon energies, thus spanning the traditional ARPES regime and extending it to soft and hard x-ray ARPES. The validity of this approach has been demonstrated with illustrative soft and hard x-ray calculations for Au and Pt, and by direct comparison to experimental soft x-ray data from W(110). Our approach correctly converges at high energy and/or temperature to the so-called XPS or MEW-DOS limit, as demonstrated in the calculations for Au and Pt. Furthermore, we were able to show that this limit is triggered mainly by temperature-dependent relaxation of the usual  $\mathbf{k}$ -conservation selection rules. The nearly quantitative agreement between experiment and theory further illustrates that our approach could work as a powerful analysis tool for various soft x-ray as well as hard x-ray ARPES investigations in the future.

#### ACKNOWLEDGMENTS

Financial support by the Deutsche Forschungsgemeinschaft through FOR 1346, EB-154/20, EBE-154/23, EBE-154/26-1, Projekt SPP 1666, MI-1327/1 and by the Bundesministerium für Bildung und Forschung through BMBF:05K10WMA and BMBF:05K13WMA is gratefully acknowledged. C.S.F. also acknowledges the support of the US Department of Energy under Contract No. DE-AC02-05CH11231.

#### APPENDIX

##### 1. LSDA treatment of disordered alloys

First we shortly review the coherent potential approximation (CPA)<sup>41,42</sup> within the local spin-density approximation (LSDA) scheme. The CPA is considered to be the best theory among the so-called single-site (local) alloy theories that assume complete random disorder and ignore short-range order. This scheme is implemented within the spin-polarized Korringa-Kohn-Rostoker (SPR-KKR) method.<sup>34,43</sup> Within the CPA the configurationally averaged properties of a disordered alloy are represented by a hypothetical ordered CPA medium, which in turn may be described by a corresponding site-diagonal scattering path operator  $\tau^{\text{CPA}}$ , which in turn is

closely connected with the electronic Green's function. The corresponding single-site  $t$ -matrix  $t^{\text{CPA}}$  and multiple scattering path operator  $\tau^{\text{CPA}}$  are determined by the so-called CPA condition:

$$x_A \tau^A + x_B \tau^B = \tau^{\text{CPA}}. \quad (\text{A1})$$

For example for a binary system  $A_x B_{1-x}$  composed of components A and B with relative concentrations  $x_A = x$  and  $x_B = (1 - x)$  is considered. The above equation represents the requirement that embedding substitutionally an atom (of type A or B) into the CPA medium should not cause additional scattering. The scattering properties of an A atom embedded in the CPA medium are represented by the site-diagonal component-projected scattering path operator  $\tau^A$  (angular momentum index omitted here)

$$\tau^A = \mathcal{D}^A \tau^{\text{CPA}}. \quad (\text{A2})$$

A corresponding equation holds also for the B component embedded into the CPA medium. The coupled sets of equations for  $\tau^{\text{CPA}}$  and  $t^{\text{CPA}}$  have to be solved iteratively within the CPA cycle. The factor  $\mathcal{D}^A = [1 + (t_A^{-1} - \tau_{\text{CPA}}^{-1})]^{-1}$  in Eq. (15) is called the CPA projector. The quantities  $t^A$  and  $t^{\text{CPA}}$  denote the single-site matrices of the A component and of the CPA effective medium.

## 2. Calculation of the CPA photocurrent at $T = 0$ K

We start our considerations by giving Pendry's formula for the photocurrent which defines the one-step model of AR-PES<sup>44</sup>:

$$I^{\text{AR-PES}} \propto \text{Im} \langle \epsilon_f, \mathbf{k} | G_2^+ \Delta G_1^+ \Delta^\dagger G_2^- | \epsilon_f, \mathbf{k} \rangle. \quad (\text{A3})$$

The first step in an explicit calculation of the photocurrent consists in the setup of the relativistic spin-polarized low energy electron diffraction (SPLEED) formalism within the CPA theory. The coherent scattering matrix  $t_n^{\text{CPA}}$  for the  $n$ th atomic site together with the crystal geometry determines the scattering matrix  $M$  for a certain layer of the semi-infinite half-space:

$$\begin{aligned} M_{\mathbf{g}\mathbf{g}'}^{\tau\tau's's'} &= \delta_{\mathbf{g}\mathbf{g}'}^{\tau\tau's's'} + \frac{8\pi^2}{kk_{\mathbf{g}z}} \sum_{\substack{nn' \\ \Lambda\Lambda'\Lambda''}} i^{-l} C_{\Lambda}^{m_s} Y_l^{\mu-m_s}(\hat{\mathbf{k}}_{\mathbf{g}}^{\tau}) \\ &\times t_n^{\text{CPA}} (1-X)_{\Lambda''\Lambda'}^{-1} i^{l'} C_{\Lambda'}^{m'_s} Y_{l'}^{\mu'-m'_s}(\hat{\mathbf{k}}_{\mathbf{g}'}^{\tau'}) \\ &\times e^{-i(\mathbf{k}_{\mathbf{g}}^{\tau} \mathbf{R}_n + \mathbf{k}_{\mathbf{g}'}^{\tau'} \mathbf{R}_{n'})}. \end{aligned} \quad (\text{A4})$$

By means of the layer-doubling technique the so-called bulk-reflection matrix can be calculated, which gives the scattering properties of a semi-infinite stack of layers. Finally, applying SPLEED theory<sup>23,43</sup> we are able to derive the final state for the semi-infinite crystal. The quantity  $\Delta$  in Eq. (A3) is the dipole operator in the electric dipole approximation. It mediates the coupling of the high-energy final state with the low-energy initial states. In a fully relativistic theory the dipole interaction of an electron with the electromagnetic field is given by the dipole operator  $\Delta = -\boldsymbol{\alpha} \mathbf{A}_0$ , where  $\mathbf{A}_0$  is the spatially constant vector potential inside the crystal. The three components  $\alpha_k$  of the vector  $\boldsymbol{\alpha}$  are defined through the tensor

product  $\alpha_k = \sigma_1 \otimes \sigma_k$ ,  $k = 1, 2, 3$ , where  $\sigma_k$  denote the Pauli spin matrices. Dealing with the matrix element  $\langle \Psi_f | \Delta | \Psi_i \rangle$  between eigenspinors  $|\Psi_f\rangle$  and  $|\Psi_i\rangle$  of the Dirac Hamiltonian with energies  $E_f$  and  $E_i$ , respectively, it is more convenient to express  $\Delta$  in the equivalent form

$$\begin{aligned} \Delta &= E \left( \mathbf{A}_0 \nabla + \frac{i\omega}{c} \boldsymbol{\alpha} \mathbf{A}_0 \right) V_{\text{LSDA}} + E (\mathbf{A}_0 \nabla) \beta \boldsymbol{\sigma} \mathbf{B}_{\text{LSDA}} \\ &+ E \frac{\omega}{c} \beta \mathbf{A}_0 \times \boldsymbol{\sigma} \mathbf{B}_{\text{LSDA}}, \end{aligned} \quad (\text{A5})$$

with  $E = -2ic/[(E_f + c^2)^2 - (E_i + c^2)^2]$ . The expression is derived by making use of commutator and anticommutator rules analogously to the nonrelativistic case in Ref. 45. The quantity  $V_{\text{LSDA}}$  denotes the spin-independent potential, and  $\mathbf{B}_{\text{LSDA}}$  is the effective magnetic field. They are given as

$$V_{\text{LSDA}} = \frac{1}{2}(V_{\text{LSDA}}^{\uparrow} + V_{\text{LSDA}}^{\downarrow}) \quad (\text{A6})$$

and

$$\mathbf{B}_{\text{LSDA}} = \frac{1}{2}(V_{\text{LSDA}}^{\uparrow} - V_{\text{LSDA}}^{\downarrow}) \mathbf{b}. \quad (\text{A7})$$

The constant unit vector  $\mathbf{b}$  determines the spatial direction of the (uniform) magnetization as well as the spin quantization axis.  $\beta$  denotes the usual  $4 \times 4$  Dirac matrix with the nonzero diagonal elements  $\beta_{11} = \beta_{22} = 1$  and  $\beta_{33} = \beta_{44} = -1$ .

According to Pendry<sup>44</sup> the calculation of  $G_1^+$ , and in consequence the calculation of the photocurrent, can be divided into four different steps. The first contribution  $I^{\text{at}}$ , the so called "atomic contribution", results from the replacement of  $G_1^+$  in Eq. (A3) by  $G_{1,a}^+$ . The second contribution  $I^{\text{ms}}$  describes the multiple scattering of the initial state. The third contribution  $I^s$  to the photocurrent takes care of the surface. When dealing with the disorder in the alloys, an additional  $I^{\text{inc}}$ , the so called "incoherent" term, appears. Following Durham *et al.*<sup>30,31</sup> the configurational average can be written as

$$\langle I^{\text{AR-PES}} \rangle = \frac{1}{\pi} \text{Im} \sum_{ij} \langle M_i \tau^{ij} M_j^* \rangle - \frac{1}{\pi} \text{Im} \sum_i \langle M_i^a \rangle + \langle I^s \rangle. \quad (\text{A8})$$

Herein  $\tau^{ij}$  denotes the scattering path operator between the sites  $i$  and  $j$ .  $M_i^a$  represents an atomic-type matrix element containing the irregular solutions which appear as a part of the retarded Green function  $G_{1,a}^+$ .  $M_i$  indicates a conventional matrix element between regular solutions of the initial and final states. The first term can be decomposed in on-site and off-site contributions:

$$\sum_{ij} \langle M_i \tau^{ij} M_j^* \rangle = \sum_{i,j,i \neq j} \langle M_i \tau^{ij} M_j^* \rangle + \sum_i \langle M_i \tau^{ii} M_i^* \rangle. \quad (\text{A9})$$

The on-site term is called the incoherent part of the photocurrent since this term reveals density-of-states (DOS)-like behavior by definition. The off-site contribution, which contains all dispersing features, represents the so-called coherent part of the photocurrent. Together with the surface part that remains unchanged by the averaging procedure  $\langle I^s \rangle = I^s$  the

total one-step current can be written as

$$\begin{aligned} \langle I^{\text{AR-PES}} \rangle = & -\frac{1}{\pi} \text{Im} \sum_i \langle M_i^a \rangle + I^s \\ & + \frac{1}{\pi} \text{Im} \sum_{ij, i \neq j} \langle M_i \tau^{ij} M_j^* \rangle \\ & + \frac{1}{\pi} \text{Im} \sum_i \langle M_i \tau^{ii} M_i^* \rangle. \end{aligned} \quad (\text{A10})$$

Using Pendry's notation it follows:

$$\begin{aligned} \langle I^{\text{AR-PES}}(\epsilon_f, \mathbf{k}) \rangle = & \langle I^{\text{at}}(\epsilon_f, \mathbf{k}) \rangle + \langle I^{\text{ms}}(\epsilon_f, \mathbf{k}) \rangle \\ & + \langle I^{\text{inc}}(\epsilon_f, \mathbf{k}) \rangle + I^s(\epsilon_f, \mathbf{k}), \end{aligned} \quad (\text{A11})$$

where  $I^{\text{ms}}$  can be identified with the coherent contribution that describes all bandlike features of the initial state and  $I^{\text{inc}}$  with the incoherent contribution that describes the corresponding DOS-like features. Because of this clear cut separation in contributions that describe dispersing or nondispersing features one may easily define the angle-integrated photocurrent by use of the CPA formalism. The ordered case is then defined by an binary alloy with two identical species at each atomic site. Therefore, it follows:

$$\langle I^{\text{AL-PES}}(\epsilon_f, \mathbf{k}) \rangle = \langle I^{\text{at}}(\epsilon_f, \mathbf{k}) \rangle + \langle I^{\text{inc}}(\epsilon_f, \mathbf{k}) \rangle + I^s(\epsilon_f, \mathbf{k}). \quad (\text{A12})$$

For the atomic contribution the averaging procedure is trivial since  $\langle I^{\text{at}}(\epsilon_f, \mathbf{k}) \rangle$  is a single site quantity. In detail, the atomic contribution is built up by a product between the matrix  $\mathcal{Z}_{jn\alpha_n}^{\text{at}}$  and the coherent multiple scattering coefficients  $A_{jn\Lambda}^c$  of the final state. Herein  $n$  denotes the  $n$ th cell of the  $j$ th layer and  $\Lambda$  denotes the combined relativistic quantum numbers  $(\kappa, \mu)$ . It follows:

$$\langle I^{\text{at}}(\epsilon_f, \mathbf{k}) \rangle \propto \text{Im} \sum_{jn\alpha_n} x_{jn\alpha_n} A_{jn\Lambda}^c \mathcal{Z}_{jn\alpha_n}^{\text{at}} A_{jn\Lambda'}^{c*}, \quad (\text{A13})$$

where  $\alpha_n$  denotes the different atomic species located at a given atomic site  $n$  of the  $j$ th layer. The corresponding concentration is given by  $x_{jn\alpha_n}$ .

For an explicit calculation  $\mathcal{Z}^{\text{at}}$  must be separated into angular matrix elements and radial double matrix elements. A detailed description of the matrix  $\mathcal{Z}^{\text{at}}$  and of the multiple scattering coefficients  $A_{jn\Lambda}^c$  for the different atomic species is given in Refs. 33 and 46.

The intra(inter)-layer contributions  $\langle I^{\text{ms}}(\epsilon_f, \mathbf{k}) \rangle$  to the photocurrent describe the multiple scattering corrections of the initial state  $G_1^+$  between and within the layers of the single crystal. They can be written in a similar form:

$$\langle I^{\text{ms}}(\epsilon_f, \mathbf{k}) \rangle \propto \text{Im} \sum_{jn\alpha_n} A_{jn\Lambda}^c \mathcal{Z}_{jn\alpha_n}^{c(2)} C_{jn\Lambda'}^{B,G}. \quad (\text{A14})$$

In analogy to the atomic contribution the coherent matrix  $\mathcal{Z}^{c(2)}$  can be separated into angular and radial parts. The difference to the atomic contribution is that the radial part of the matrix  $\mathcal{Z}^{c(2)}$  consists of radial single matrix elements instead of radial double integrals. In the alloy case this matrix results in the

following expression:

$$\mathcal{Z}_{jn\alpha_n}^{c(2)} = \sum_{\alpha_n} x_{jn\alpha_n} D_{\Lambda_1\Lambda_2} R_{jn\alpha_n}^{(2)} \mathcal{D}_{jn\alpha_n} \cdot \quad (\text{A15})$$

The radial and angular parts of the matrix element are denoted by  $R^{(2)}$  and  $D$ . The CPA-average procedure explicitly is represented in terms of the CPA-projector  $\mathcal{D}_{jn\alpha_n}$  representing the  $\alpha$  species at site  $n$  for layer  $j$ .  $C^B$  and  $C^G$  denote the coherent multiple scattering coefficients of the initial state within a layer and between different layers. They have the form

$$C_{jn\Lambda}^B = \sum_{n'\Lambda'\Lambda''} B_{jn'\Lambda'}^{(o)c} (t^{\text{CPA}})^{-1}_{jn'\Lambda'} \left( (1-X)^{-1}_{jn\Lambda} - \delta_{nn'} \right), \quad (\text{A16})$$

with the coherent bare amplitudes  $B_{jn'\Lambda'}^{(o)c}$ :

$$B_{jn'\Lambda'}^{(o)c} = \sum_{\Lambda''} \mathcal{Z}_{jn'\Lambda'}^{c(1)} A_{jn'\Lambda''}^{c*} \quad (\text{A17})$$

and

$$\mathcal{Z}_{jn\Lambda'}^{c(1)} = \sum_{\alpha_n} x_{jn\alpha_n} \mathcal{D}_{jn\alpha_n}^\dagger R_{jn\alpha_n}^{(1)} D_{\Lambda_1\Lambda_2}^\dagger. \quad (\text{A18})$$

Finally, the coherent scattering coefficients  $C^G$  for the interlayer contribution take the form

$$C_{jn\Lambda}^G = \sum_{n'\Lambda'} G_{jn'\Lambda'}^{(o)c} (1-X)^{-1}_{jn'n} \quad (\text{A19})$$

and the coherent bare amplitudes  $G_{jn'\Lambda'}^{(o)c}$  are given by

$$\begin{aligned} G_{jn'\Lambda'}^{(o)c} = & \sum_{\mathbf{g}m_s} 4\pi i^{l'} (-)^{l'-s} C_{\Lambda'}^{m_s} [d_{j\mathbf{g}m_s}^+ Y_{l'}^{m_s-\mu'}(\widehat{k}_{1\mathbf{g}}^+) e^{i\mathbf{k}_{1\mathbf{g}}^+ \cdot \mathbf{r}_{n'}} \\ & + d_{j\mathbf{g}m_s}^- Y_{l'}^{m_s-\mu'}(\widehat{k}_{1\mathbf{g}}^-) e^{i\mathbf{k}_{1\mathbf{g}}^- \cdot \mathbf{r}_{n'}}]. \end{aligned} \quad (\text{A20})$$

The coefficients  $d_{j\mathbf{g}m_s}^\pm$  in Eq. (A20) represent the plane-wave expansion of the initial state between the different layers of the semi-infinite stack of layers. For a detailed description of the matrices  $\mathcal{Z}^{\text{at}}$ ,  $\mathcal{Z}^{(1)}$ , and  $\mathcal{Z}^{(2)}$  and of the multiple scattering coefficients  $d_{j\mathbf{g}m_s}^\pm$  the reader again is referred to Refs. 33 and 46.

The last contribution to the alloy photocurrent is the so called incoherent part  $\langle I^{\text{inc}}(\epsilon_f, \mathbf{k}) \rangle$ , which appears because the spectral function of an disordered alloy<sup>42</sup> is defined as a non-single-site quantity. In fact, this contribution is closely connected with the presence of the irregular wave functions well known from the spherical representation of the Green function  $G_1^+$ . The incoherent term is defined as

$$\begin{aligned} \langle I^{\text{inc}}(\epsilon_f, \mathbf{k}) \rangle \propto & \text{Im} \sum_{jn\alpha_n} x_{jn\alpha_n} A_{jn\Lambda}^c \mathcal{Z}_{jn\alpha_n}^{(1)} \\ & * (\tau_{jn\alpha_n}^{00} - t_{jn\alpha_n})_{\Lambda'\Lambda''} \mathcal{Z}_{jn\alpha_n}^{(2)} A_{jn\Lambda''}^{c*} \\ & + \text{Im} \sum_{jn\alpha_n} A_{jn\Lambda}^c \mathcal{Z}_{jn\alpha_n}^{c(1)} \tau_{cjn}^{00} \mathcal{Z}_{jn\alpha_n}^{c(2)} A_{jn\Lambda''}^{c*}, \end{aligned} \quad (\text{A21})$$



at which  $\tau_{jn\alpha_n}^{00}$  denotes the one-site restricted average CPA matrix for species  $\alpha_n$  at atomic site  $n$  for layer  $j$ .  $\tau_{cjn}^{00}$  represents the corresponding matrix for the coherent

medium. The incoherent part  $\langle I^{\text{inc}}(\epsilon_f, \mathbf{k}) \rangle$  completes the CPA-averaged photocurrent within the fully relativistic one-step model.

- <sup>1</sup>A. Damascelli, Z. Hussain, and Z. X. Shen, *Rev. Mod. Phys.* **75**, 473 (2003).
- <sup>2</sup>D. H. Lu, I. M. Vishik, M. Yi, Y. Chen, R. G. Moore, and Z. X. Shen, *Annu. Rev. Cond. Mat. Phys.* **3**, 129 (2012).
- <sup>3</sup>S. Tanuma, C. J. Powell, and D. R. Penn, *Surf. Interface Anal.* **43**, 689 (2011).
- <sup>4</sup>Z. Hussain, C. S. Fadley, S. Kono, and L. F. Wagner, *Phys. Rev. B* **22**, 3750 (1980).
- <sup>5</sup>Ch. Søndergaard, Ph. Hofmann, Ch. Schultz, M. S. Moreno, J. E. Gayone, M. A. V. Alvarez, G. Zampieri, S. Lizzit, and A. Baraldi, *Phys. Rev. B* **63**, 233102 (2001).
- <sup>6</sup>A. Sekiyama and S. Suga, *J. Electron Spectrosc. Relat. Phenom.* **137**, 681 (2004).
- <sup>7</sup>A. Yamasaki, A. Sekiyama, S. Imada, M. Tsunekawa, A. Higashiya, A. Shigemoto, and S. Suga, *Nucl. Instrum. Methods Phys. Res. Sect. A* **547**, 136 (2005).
- <sup>8</sup>T. Yokoya, T. Nakamura, T. Matsushita, T. Muro, Y. Takano, M. Nagao, T. Takenouchi, H. Kwarada, and T. Oguchi, *Nature (London)* **438**, 647 (2005).
- <sup>9</sup>M. Yano, A. Sekiyama, H. Fujiwara, T. Saita, S. Imada, T. Muro, Y. Onuki, and S. Suga, *Phys. Rev. Lett.* **98**, 036405 (2007).
- <sup>10</sup>L. Plucinski, J. Minár, B. C. Sell, J. Braun, H. Ebert, C. M. Schneider, and C. S. Fadley, *Phys. Rev. B* **78**, 035108 (2008).
- <sup>11</sup>F. Venturini, J. Minár, J. Braun, H. Ebert, and N. B. Brookes, *Phys. Rev. B* **77**, 045126 (2008).
- <sup>12</sup>S. Suga and A. Sekiyama, *J. Electron Spectrosc. Relat. Phenom.* **181**, 48 (2010).
- <sup>13</sup>A. X. Gray, C. Papp, S. Ueda, B. Balke, Y. Yamashita, L. Plucinski, J. Minár, J. Braun, E. R. Ylvisaker, C. M. Schneider, W. E. Pickett, H. Ebert, K. Kobayashi, and C. S. Fadley, *Nat. Mater.* **10**, 759 (2011); accompanying News and Views, D. L. Feng, *ibid.* **10**, 729 (2011).
- <sup>14</sup>C. S. Fadley, *Synchrotron Radiat. News* **25**, 26 (2012).
- <sup>15</sup>V. N. Strocov, M. Shi, M. Kobayashi, C. Monney, X. Wang, J. Krempasky, Th. Schmitt, L. Patthey, H. Berger, and P. Blaha, *Phys. Rev. Lett.* **109**, 086401 (2012).
- <sup>16</sup>A. X. Gray, J. Minár, S. Ueda, P. R. Stone, Y. Yamashita, J. Fujii, J. Braun, L. Plucinski, C. M. Schneider, G. Panaccione, H. Ebert, O. D. Dubon, K. Kobayashi, and C. S. Fadley, *Nat. Mater.* **11**, 957 (2012).
- <sup>17</sup>G. Landolt, S. V. Ereemeev, Y. M. Koroteev, B. Slomski, S. Muff, T. Neupert, M. Kobayashi, V. N. Strocov, Th. Schmitt, Z. S. Aliev, M. B. Babanly, I. R. Amiraslanov, E. V. Chulkov, J. Osterwalder, and J. H. Dil, *Phys. Rev. Lett.* **109**, 116403 (2012).
- <sup>18</sup>J. Minár, J. Braun, and H. Ebert, *J. Electron. Spectrosc. Relat. Phenom.* (2013), doi: 10.1016/j.elspec.2013.06.008.
- <sup>19</sup>J. Fujii, B. R. Salles, M. Sperl, S. Ueda, M. Kobata, K. Kobayashi, Y. Yamashita, P. Torelli, M. Utz, C. S. Fadley, A. X. Gray, J. Braun, H. Ebert, I. Di Marco, O. Eriksson, P. Thunström, G. H. Fecher, H. Stryhanyuk, E. Ikenaga, J. Minár, C. H. Back, G. Van der Laan, and G. Panaccione, *Phys. Rev. Lett.* **111**, 097201 (2013).
- <sup>20</sup>A. X. Gray, J. Minár, L. Plucinski, M. Huijben, A. Bostwick, E. Rotenberg, S.-H. Yang, J. Braun, A. Winkelman, G. Conti, D. Eiteneer, A. Rattanachata, A. A. Greer, J. Ciston, C. Ophus, G. Rijnders, D. H. A. Blank, D. Doenning, R. Pentcheva, J. B. Kortright, C. M. Schneider, H. Ebert, and C. S. Fadley, *Europhys. Lett.* **104**, 17004 (2013).
- <sup>21</sup>M. Kobayashi, I. Muneta, Y. Takeda, Y. Harada, A. Fujimori, J. Krempasky, Th. Schmitt, S. Ohya, M. Tanaka, M. Oshima, and V. N. Strocov, arXiv:1302.0063.
- <sup>22</sup>N. J. Shevchik, *Phys. Rev. B* **16**, 3428 (1977).
- <sup>23</sup>R. Feder, *J. Phys. C* **14**, 2049 (1981).
- <sup>24</sup>R. Paniago, R. Matzdorf, G. Meister, A. Goldmann, J. Braun, and G. Borstel, *Surf. Sci.* **347**, 46 (1996).
- <sup>25</sup>C. G. Larrison and J. B. Pendry, *J. Phys. C: Solid State Phys.* **14**, 3089 (1981).
- <sup>26</sup>M. A. V. Alvarez, H. Ascolani, and G. Zampieri, *Phys. Rev. B* **54**, 14703 (1996).
- <sup>27</sup>T. Fujikawa and H. Arai, *J. Electron. Spectrosc. Relat. Phenom.* **174**, 85 (2009).
- <sup>28</sup>T. Fujikawa, *J. Electron. Spectrosc. Relat. Phenom.* **173**, 51 (2009).
- <sup>29</sup>C. Papp, L. Plucinski, J. Minár, J. Braun, H. Ebert, C. M. Schneider, and C. S. Fadley, *Phys. Rev. B* **84**, 045433 (2011).
- <sup>30</sup>P. J. Durham, *J. Phys. F: Met. Phys.* **11**, 2475 (1981).
- <sup>31</sup>B. Ginatempo, P. J. Durham, and B. I. Gyorffy, *J. Phys.: Condens. Matter* **1**, 6483 (1989).
- <sup>32</sup>J. Braun, J. Minár, F. Matthes, C. M. Schneider, and H. Ebert, *Phys. Rev. B* **82**, 024411 (2010).
- <sup>33</sup>J. Braun, *Rep. Prog. Phys.* **59**, 1267 (1996).
- <sup>34</sup>H. Ebert *et al.*, The munich SPR-KKR package, version 6.3, [<http://olymp.cup.uni-muenchen.de/ak/eibert/SPRKKR>] (2012).
- <sup>35</sup>H. Ebert, S. Mankovsky, D. Ködderitzsch, and P. J. Kelly, *Phys. Rev. Lett.* **107**, 066603 (2011).
- <sup>36</sup>H. Ebert, D. Ködderitzsch, and J. Minár, *Rep. Prog. Phys.* **74**, 096501 (2011).
- <sup>37</sup>J. Minár, J. Braun, S. Mankovsky, and H. Ebert, *J. Elect. Spectrosc. Relat. Phenom.* **184**, 91 (2011).
- <sup>38</sup>A. X. Gray, J. Karel, J. Minár, C. Bordel, H. Ebert, J. Braun, S. Ueda, Y. Yamashita, L. Ouyang, D. J. Smith, K. Kobayashi, F. Hellman, and C. S. Fadley, *Phys. Rev. B* **83**, 195112 (2011).
- <sup>39</sup>J. Braun, J. Minár, H. Ebert, A. Chainani, J. Miyawaki, Y. Takata, M. Taguchi, M. Oura, and S. Shin, *Phys. Rev. B* **85**, 165105 (2012).
- <sup>40</sup>J. B. Pendry, *Low Energy Electron Diffraction* (Academic, London, 1974).
- <sup>41</sup>P. Soven, *Phys. Rev.* **156**, 809 (1967).
- <sup>42</sup>J. S. Faulkner and G. M. Stocks, *Phys. Rev. B* **21**, 3222 (1980).
- <sup>43</sup>J. Korringa, *Physica* **6/7**, 392 (1947); W. Kohn and N. Rostoker, *Phys. Rev.* **94**, 1111 (1954).
- <sup>44</sup>J. B. Pendry, *Surf. Sci.* **57**, 679 (1976).
- <sup>45</sup>M. Potthoff, J. Lachnitt, W. Nolting, and J. Braun, *Phys. Status Solidi B* **203**, 441 (1997).
- <sup>46</sup>J. Braun, in *Band-Ferromagnetism: Ground-State and Finite-Temperature Phenomena*, edited by K. Baberschke, M. Donath, and W. Nolting (Springer, New York, 2001), p. 267.